Journal of the Mechanics and Physics of Solids 122 (2019) 538–554

Contents lists available at ScienceDirect

Journal of the Mechanics and Physics of Solids

journal homepage: www.elsevier.com/locate/jmps

Thermoelastic deformation and failure of rubberlike materials

Y. Lev[a,*], A. Faye[b], K.Y. Volokh[a]

[a] Faculty of Civil and Environmental Engineering, Technion, Haifa, Israel
[b] Department of Mechanical Engineering, Indian Institute of Technology, Bhilai, India

ARTICLE INFO

Article history:
Received 6 May 2018
Revised 26 September 2018
Accepted 26 September 2018
Available online 1 October 2018

Keywords:
Rubberlike materials
Thermoelasticity
Failure
Cavitation
Energy limiter

ABSTRACT

In many practical applications rubber components are exposed to relatively high operating temperatures yet very few studies can be found in the literature that deal with the temperature influence on deformation and, especially, failure of rubberlike materials. In the present work, we partly fill this gap providing the experimental results on uniaxial tension and bulge tests for nitrile butadiene rubber, neoprene, and silicone for various temperatures in the range from 20°C to 90°C. Based on the results of the tests we develop novel thermoelastic constitutive models, which also incorporate a failure description via the method of energy limiters. Using the developed models, we study the cavitation problem under the elevated temperatures. We find that, generally, the heating might lower material strength while the material stiffness is not necessarily sensitive to the temperature alterations.

1. Introduction

Rubberlike materials and structures might be exposed to heating between 20°C and 90°C in the rubbery state. For example, the temperature alterations can naturally occur at the tip of a propagating crack, which would affect the fracture process. The heating, in its turn, can change material properties - stiffness and strength. The latter effect is the target of the experimental studies and theoretical models reported in the present work.

Coupled thermal and elastic deformations - thermoelasticity - of rubberlike materials is not a new subject yet the data concerning both experiment and theory are quite limited (Aboudi, 2002; Chadwick, 1974; Chadwick and Creasy, 1984; Dickie and Smith, 1969; Holzapfel, 2000; Lev et al., 2018; Morman Jr, 1995; Ogden, 1992; Saccomandi and Ogden, 2004; Volokh, 2015). Physical and geometrical nonlinearities inherent in rubberlike materials present a natural difficulty for experiments and theory. For example, a constitutive model calibrated in uniaxial tension tests might fail to properly describe biaxial stress-stretch conditions and vise versa (Marckmann and Verron, 2006).

In the present work, we examine the three rubberlike materials that were previously mentioned in Lev et al. (2018). These materials are commonly used in automotive, electronics and construction industries for a wide range of applications including load bearings, fuel and oil handling hoses, seals, grommets and self-sealing fuel tanks (Gent, 2001; Rodgers, 2015): (a) Nitrile Butadiene Rubber (NBR), which is Sulfur vulcanized with Shore 41A, mass density of 1.14 g/cm^3, and the glass transition and melting temperatures of −35°C and 100°C accordingly; (b) Neoprene, which is Sulfur vulcanized with Shore 35A, mass density of 1.33 g/cm^3, and the glass transition and melting temperatures of −55°C and 100°C accordingly;

* Corresponding author.
E-mail address: yoavlev@campus.technion.ac.il (Y. Lev).

https://doi.org/10.1016/j.jmps.2018.09.033
0022-5096/

(c) Silicone rubber, which is Peroxide vulcanized with Shore 41A, mass density of 1.13 g/cm^3, and the glass transition and melting temperatures of -60°C and 200°C accordingly.[1]

We perform both uniaxial and biaxial tests. The latter tests are not direct and use the balloon inflation technique - the bulge test (Charalambides et al., 2002; Hamdi et al., 2006; Lev et al., 2018; Sasso et al., 2008). Both types of tests are done using the same portion for each material. The material specimens are exposed to the temperatures 25°C, 50°C, 70°C, 90°C during time not exceeding half an hour.

We use the experimental data to develop and calibrate the thermo-hyperelastic theoretical models enhanced with the energy limiter to describe material failure. The limiter indicates the maximum failure energy that can be stored by an infinitesimal material volume (Volokh, 2007; 2010; 2013; 2015). As opposed to the previous work done in Lev et al. (2018) that considered only bulge tests, we now add also the uniaxial case which allows to produce a more general set of material parameters.

The parameters are derived via a non-linear least squares minimization procedure as done in Ogden et al. (2004). This procedure enables to fit multiple sets of data simultaneously. The objective function includes two sets of data from uniaxial and bulge tests. The data-fitting is based on the Matlab non-linear least squares optimization tool (MATLAB, 2017). The three-term Ogden model was chosen after it was found that the Yeoh model, used in Lev et al. (2018), failed to reach an adequate simultaneous correlation level. This indicates the relatively strong advantage of the Ogden model. Performing the simultaneous fit is important since rubber-like materials may be subjected to different biaxial stretch ratios. Calibration based on only one load configuration can lead to an engineering error. Despite this fact, apparently because of the simplicity of the method, most manufactures do a calibration according to uniaxial tests only.

A new constitutive relation for the thermal energy contribution is developed. In contrast to the calibration done in Lev et al. (2018), we present here a fit using the coupled thermo-elastic theory displayed. A new relation for the temperature dependence on the energy limiters is derived.

Calibrated material models are further used to calculate the critical hydrostatic tension indicating the onset of cavitation in the considered materials under the varying temperatures. The results of the cavitation analyses depend on the temperature through both the material stiffness and strength. The latter correlation is not surprising because cavitation is a material failure phenomenon.

2. Experiments

Rubberlike materials can have fairly large uniaxial stretches ($\sim 7-8$) before they fail, which makes it difficult to test them under temperature controlled environment. Most environmental chambers integrated with commercially available load frames are not suitable to accommodate such large stretches (ASTM, 2007; Vahapoglu et al., 2011). To overcome this issue we have prepared uniaxial and equibiaxial test setups with temperature controlled environment that can accommodate sufficiently large stretches. Both uniaxial and equibiaxial test setups are placed inside a chamber made of Polycarbonate sheets. Walls of the chamber are insulated from inside to prevent heat loss. The temperature inside the chamber is controlled by using a hot-air blower with integrated temperature control. Several thermocouples are placed appropriately to ensure a constant and uniform temperature inside the chamber. The tests are performed for three different rubber materials; (a) NBR, (b) Neoprene, and (c) Silicone. For each material, tests are conducted under a constant temperature environment at four different temperatures, 25°C, 50°C, 70°C, 90°C. Average thickness of the specimens for NBR, Neoprene, and Silicone are about 1.2, 1.2 and 1.1 mm, respectively (measured by a caliper).

2.1. Uniaxial tension test

The setup for conducting the uniaxial test at a constant temperature environment is shown in Fig. 1.

The dumbbell shaped specimen used for the uniaxial test is shown in Fig. 2.

The specimen is gripped tightly at the upper and lower grip section. The upper grip is attached to the frame and remain fixed, whereas the lower grip is pulled by metallic wires connected to a rotating shaft. Two metalic wires attach the lower grip. These cables pass through two matching holes in the floor of the chamber. This connection guides the wires and prevents the lower grip and as a result the dumbbell from rotating. The shaft (diameter 12 mm) is mounted on the bearings and connected to a DC motor rotating at a constant angular velocity of 1 rpm. The specimen is thus pulled at a speed of 40 mm/min. A S-type load cell (Capacity: 250 lb at 3.7532 mV/V) is connected in series with the specimen (as shown in Fig. 1) to measure the load experienced by the specimen. The elongation of the gauge section is measured using laser displacement measurement sensors (Range: 150–1000 mm $\pm$ 0.5 mm on the max range). The laser is a low class number 2 laser. Two clips with laser reflective labels are attached at the two ends of the gauge length. The labels are perpendicular to the direction of loading and reflects the laser beam transmitted by the sensors placed above the chamber. The sensors detect the reflected laser beams and measure the displacement of the two end points of the gauge section. The lasers are aimed at the center of the labels close to the dumbbell so that the measured displacements from the two labels are not affected by slight rotations of the labels that may occur throughout the test. The difference between the two displacements

[1] All three rubber materials were purchased from “GUMIAN rubber products LTD”.

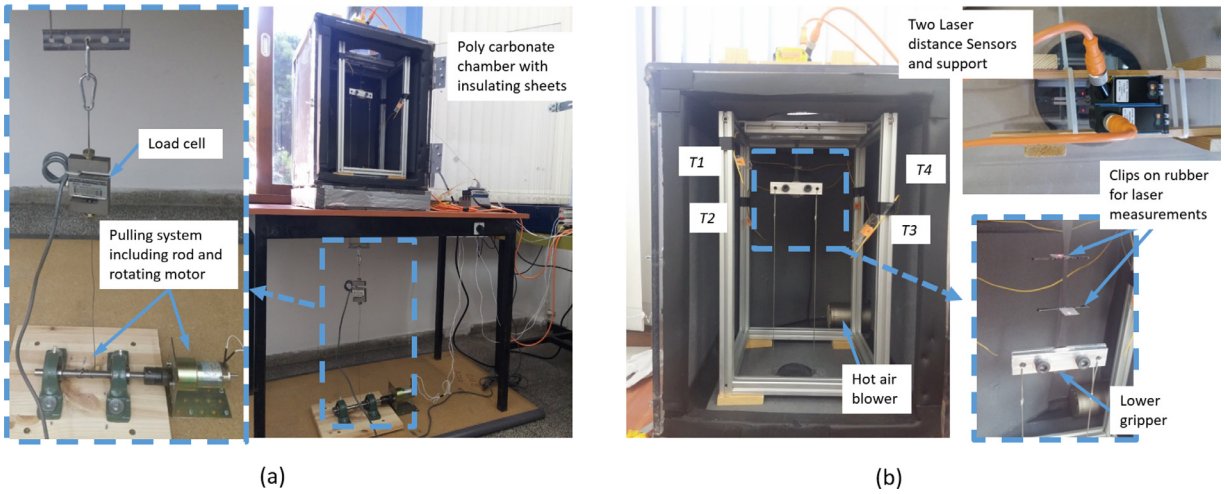

Fig. 1. Experimental setup for the uniaxial tension test.

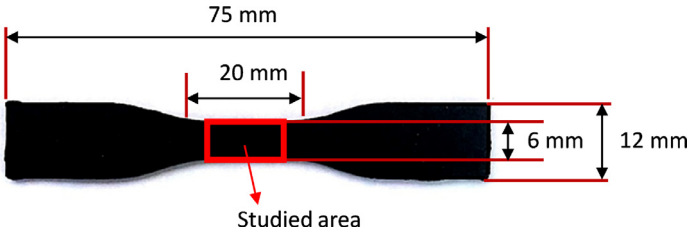

Fig. 2. Dimensions of Dumbbell rubber specimen for the uniaxial tension test.

gives the elongation of the gauge section. The tests are done up to failure taking into account only the experiments that fail between the two ends of the gauge length at the studied area.

Both the load cell and laser displacement sensors are placed outside the chamber to eliminate the effects of temperature on them.

2.2. Bulge test

For the equibiaxial tests we adapt the well-known "bulge test" procedure (Charalambides et al., 2002; Hamdi et al., 2006; Sasso et al., 2008). The reader is referred to our previous publication (Lev et al., 2018) for a more detailed description of the Bulge test procedure used. For the sake of convenience we repeat the main description of the bulge test. The bulge device and schematic view of this set-up is shown in Fig. 3 (a) and (b) accordingly.

The setup of the bulge test at a constant environmental temperature is shown in Fig. 4.

Five thermocouples are placed inside the chamber, one at each side of a wall, named T_1 to T_4, and an additional thermocouple, T_5, that is placed inside the bulge device (through channel B), as shown in Fig. 4(b). This allows monitoring also the temperature inside the inflating balloon. A rubber sheet specimen is clamped between the top and the middle flanges of the bulge device (Fig. 3(a)). Temperature control inside the inflating balloon is obtained by placing a long and narrow preheated tube inside the chamber. Compressed air is supplied through channel A from the bottom flange. Air flows slowly inside this tube. By the time air enters the bulge device, temperatures inside and outside the inflating balloon are almost the same. Pressure (P) inside the bulge test device is measured at channel C using a pressure transducer (range $0-4$ bar with an accuracy of 0.5%). During the inflation, vertical displacement of the center of the rubber specimen of the bulge test is measured using a laser displacement measurement sensor.

The three materials, four temperature steps, and two test configuration (uniaxial and bulge test) add up to a total of 24 test cases. Each case was repeated three to five times to ensure repeatability and to extract average results. More than 100 tests all together where done throughout the work. The uniaxial and bulge tests are done using the same portion for each material. This reduces the material factor as a reason for differences in the mechanical results.

All the measurements mentioned (temperature, pressure, and displacement) are recorded using a data acquisition card, and stored using a designated LabVIEW program.

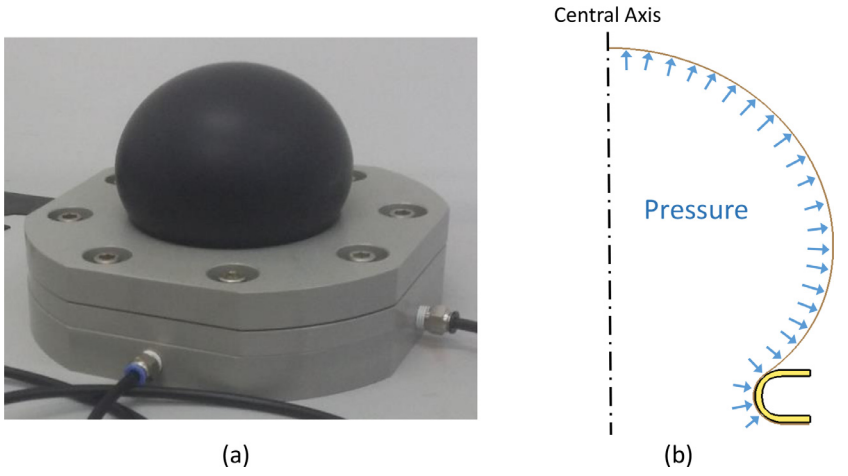

Fig. 3. (a) Bulge test device and (b) Schematic view of bulge test.

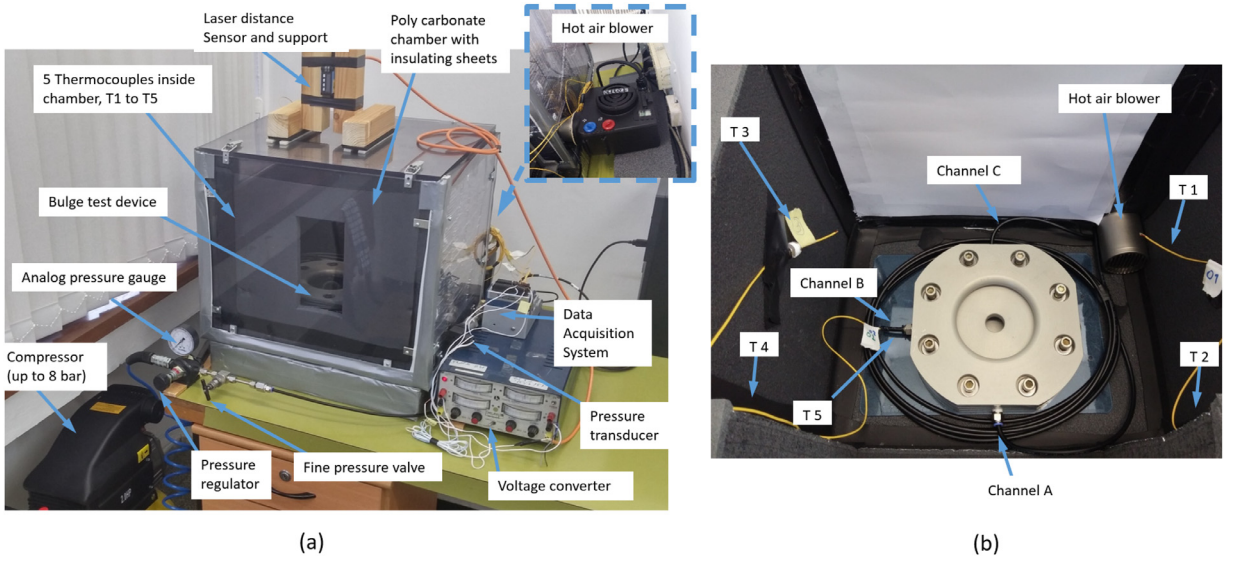

Fig. 4. Experimental setup for the bulge test.

3. Theory

We use the finite thermoelasticity theory and we refer the reader to Holzapfel (2000), Volokh (2016) for the general background.

3.1. The Helmholtz free energy

Specifically, we choose the Helmholtz free energy density in the form[2]

$$\psi(\mathbf{F}, T, \zeta) = \psi_{\mathrm{f}}(T) - H(\zeta)\psi_{\mathrm{te}}(\mathbf{F}, T), \tag{1}$$

where

$$\begin{aligned} \psi_{\mathrm{te}}(\mathbf{F}, T) &= \phi(T) m^{-1} \Gamma(m^{-1}, W(\mathbf{F}, T)^m \phi(T)^{-m}), \\ \psi_{\mathrm{f}}(T) &= \phi(T) m^{-1} \Gamma(m^{-1}, 0). \end{aligned} \tag{2}$$

and $\Gamma(s, x) = \int_x^\infty t^{s-1} e^{-t} dt$ is the upper incomplete gamma function.

[2] We generalize the theory setting of Volokh (2015) by introducing the temperature dependence of the energy limiter.

Here, we designated failure energy $\psi_{\rm f}(T)$ and thermoelastic energy $\psi_{\rm te}(\mathbf{F}, T)$ depending on the deformation gradient $\mathbf{F}$ and absolute temperature T. Material healing is prevented by the step function: $H(\zeta)=0$ if $\zeta<0$ or $H(\zeta)=1$ otherwise. The Helmholtz free energy without failure is designated by $W(\mathbf{F}, T)$ while $\phi(T)$ is the energy limiter and m is a material parameter.

We note that $\zeta\in(-\infty,0]$ is calculated from the evolution equation

$$\dot{\zeta}=-H(\epsilon-\psi_{\rm te}/\psi_{\rm f}),\quad \zeta(0)=0, \tag{3}$$

in which $0<\epsilon\ll 1$ is a precision limit.

According to (1) deformation is reversible as long as ψ is less than $\psi_{\rm f}$. The strain energy stays fixed after reaching this limit and, hence, the deformation becomes irreversible. Note that ζ is a switch function rather than internal variable: if $\zeta=0$ then the deformation is hyperelastic and if $\zeta<0$ then the deformation is irreversible.

Constitutive law for the first Piola–Kirchhoff stress tensor, $\mathbf{P}$, is derived from (1) by using a thermodynamic reasoning (Volokh, 2014)

$$\mathbf{P}=\frac{\partial\psi}{\partial\mathbf{F}}=-H\frac{\partial\psi_{\rm te}}{\partial\mathbf{F}}=H\exp[-W^m\phi^{-m}]\frac{\partial W}{\partial\mathbf{F}}. \tag{4}$$

The reader should notice that in the cases where material unloading is not relevant we can set $\zeta\equiv 0\Rightarrow H\equiv 1$.

The incompressibility condition $J=\det\mathbf{F}=1$ typical of most rubberlike materials should be modified in the case of the thermoelastic coupling as follows, for example,

$$J=\det\mathbf{F}=\exp[3\gamma_0(T-T_0)] \tag{5}$$

in order to account for the material volume alteration under heating, where γ_0 is a constant of thermal expansion.

With the latter restriction we can rewrite the constitutive Eq. (4) in the form

$$\mathbf{P}=\frac{\partial\psi}{\partial\mathbf{F}}-\kappa J\mathbf{F}^{-\rm T}, \tag{6}$$

where κ is the unknown Lagrange multiplier.

Alternatively, we may write the constitutive equation in terms of the Cauchy stress

$$\boldsymbol{\sigma}=J^{-1}\mathbf{P}\mathbf{F}^{\rm T}=J^{-1}\frac{\partial\psi}{\partial\mathbf{F}}\mathbf{F}^{\rm T}-\kappa\mathbf{1}, \tag{7}$$

where $\mathbf{1}$ is the identity tensor.

3.2. Deformations for experimental calibration

Using Cartesian basis vectors $\mathbf{e}_1$, $\mathbf{e}_2$, $\mathbf{e}_3$ and the corresponding axial stretches λ_1, λ_2, λ_3, we can specify the deformation gradient for homogeneous deformations

$$\begin{aligned}\mathbf{F}=&\lambda_1\mathbf{e}_1\otimes\mathbf{e}_1+\lambda_2\mathbf{e}_2\otimes\mathbf{e}_2+\lambda_3\mathbf{e}_3\otimes\mathbf{e}_3,\\ \lambda_1\lambda_2\lambda_3=&J(T)=\exp[3\gamma_0(T-T_0)],\end{aligned} \tag{8}$$

and, consequently, we will get only diagonal principal values of stresses

$$\begin{aligned}P_1=&\frac{\partial\psi}{\partial\lambda_1}-\kappa J\lambda_1^{-1},\\ P_2=&\frac{\partial\psi}{\partial\lambda_2}-\kappa J\lambda_2^{-1},\\ P_3=&\frac{\partial\psi}{\partial\lambda_3}-\kappa J\lambda_3^{-1}.\end{aligned} \tag{9}$$

In the case of uniaxial tension we set

$$\lambda_1=\lambda,\quad \lambda_2=\lambda_3=J^{1/2}\lambda^{-1/2}. \tag{10}$$

Further assuming $P_2=P_3=0$, we find the Lagrange multiplier

$$\kappa=J^{-1}\lambda_2\frac{\partial\psi}{\partial\lambda_2}=(J\lambda)^{-1/2}\frac{\partial\psi}{\partial\lambda_2}, \tag{11}$$

and the axial stress takes the following form

$$P=P_1=\frac{\partial\psi}{\partial\lambda_1}-J^{1/2}\lambda^{-3/2}\frac{\partial\psi}{\partial\lambda_2}. \tag{12}$$

On the other hand, we calculate

$$\frac{\partial\hat{\psi}}{\partial\lambda}=\sum_{k=1}^{3}\frac{\partial\psi}{\partial\lambda_k}\frac{\partial\lambda_k}{\partial\lambda}=\frac{\partial\psi}{\partial\lambda_1}-J^{1/2}\lambda^{-3/2}\frac{\partial\psi}{\partial\lambda_2} \tag{13}$$

where

$$\hat{\psi}(\lambda, T) = \psi(\lambda, J^{1/2}\lambda^{-1/2}, J^{1/2}\lambda^{-1/2}, T). \tag{14}$$

Substitution of (13) in (12) yields

$$P = \frac{\partial \hat{\psi}}{\partial \lambda}, \tag{15}$$

or, in terms of the Cauchy stress,

$$\sigma = \sigma_1 = J^{-1}\lambda_1 P_1 = J^{-1}\lambda \frac{\partial \hat{\psi}}{\partial \lambda}. \tag{16}$$

In the case of equibiaxial tension we have

$$\lambda_1 = \lambda_2 = \lambda, \quad \lambda_3 = J\lambda^{-2}. \tag{17}$$

Further assuming $P_3 = 0$, we find the Lagrange multiplier

$$\kappa = J^{-1}\lambda_3 \frac{\partial \psi}{\partial \lambda_3} = \lambda^{-2}\frac{\partial \psi}{\partial \lambda_3}, \tag{18}$$

and the axial stresses $P = P_1 = P_2$ take the following form

$$P = P_1 = P_2 = \frac{\partial \psi}{\partial \lambda_1} - J\lambda^{-3}\frac{\partial \psi}{\partial \lambda_3}. \tag{19}$$

Then, we calculate

$$\frac{\partial \check{\psi}}{\partial \lambda} = \sum_{k=1}^{3} \frac{\partial \psi}{\partial \lambda_k}\frac{\partial \lambda_k}{\partial \lambda} = 2\frac{\partial \psi}{\partial \lambda_1} - 2J\lambda^{-3}\frac{\partial \psi}{\partial \lambda_3}, \tag{20}$$

where

$$\check{\psi}(\lambda, T) = \psi(\lambda, \lambda, J\lambda^{-2}, T). \tag{21}$$

So, finally, we have for the equibiaxial tension

$$P = P_1 = P_2 = \frac{1}{2}\frac{\partial \check{\psi}}{\partial \lambda}, \tag{22}$$

or

$$\sigma = \sigma_1 = \sigma_2 = J^{-1}\lambda_1 P_1 = \frac{\lambda}{2J}\frac{\partial \check{\psi}}{\partial \lambda}. \tag{23}$$

The bulge test means inflation of a thin membrane. Locally, the deformation is biaxial. However, this deformation is not homogeneous and it depends on the location of the point of interest. For example, the deformation is equibiaxial on the top of the inflating membrane. Unfortunately, analytical solutions for the problem of the membrane inflation are not available and numerical finite element analysis should be done for every loading case. We refer the reader to the works (Balakhovsky and Volokh, 2012; Fried, 1982; Lev et al., 2018), for instance, where details of such analyses are presented. Obviously, the iterative parameter fit is necessary when the numerical analysis of the membrane inflation is used.

3.3. The Helmholtz free energy without failure

There is a large number of proposals to choose the strain energy for the intact behavior of rubberlike materials (Marckmann and Verron, 2006). We have chosen the three-term Ogden function (Ogden, 1972; 1997) based on the use of the principal stretches. We introduce the Helmholtz free energy function for the intact material based on the thermoelastic generalization of the Ogden model

$$\begin{aligned} W(\lambda_1, \lambda_2, \lambda_3, T) &= TT_0^{-1}W_0(\lambda_1, \lambda_2, \lambda_3) + Q(T), \\ W_0(\lambda_1, \lambda_2, \lambda_3) &= \sum_{k=1}^{3} \mu_k \alpha_k^{-1}(\lambda_1^{\alpha_k} + \lambda_2^{\alpha_k} + \lambda_2^{\alpha_k} - 3), \\ Q(T) &= c_0 T_0 \ln[T/T_0], \end{aligned} \tag{24}$$

where μ_k, α_k, and c_0 are material constants; $Q(T)$ designates the purely thermal energy; and $T \geq T_0$.

We note that the purely thermal energy $Q(T)$ is *concave and positive* and, consequently, we have for the heat capacity

$$c = -T\frac{\partial^2 W}{\partial T^2} = -T\frac{\partial^2 Q}{\partial T^2} = c_0\frac{T_0}{T} > 0. \tag{25}$$

Table 1
Material constants for the heat capacity calibration.

μ_1[MPa]	μ_2[MPa]	μ_3[MPa]	α_1	α_2	α_3	T_0[K]	γ_0[1/K]
0.63	0.0012	−0.01	1.3	5.0	−2.0	293.15	$22.333 \cdot 10^{-5}$

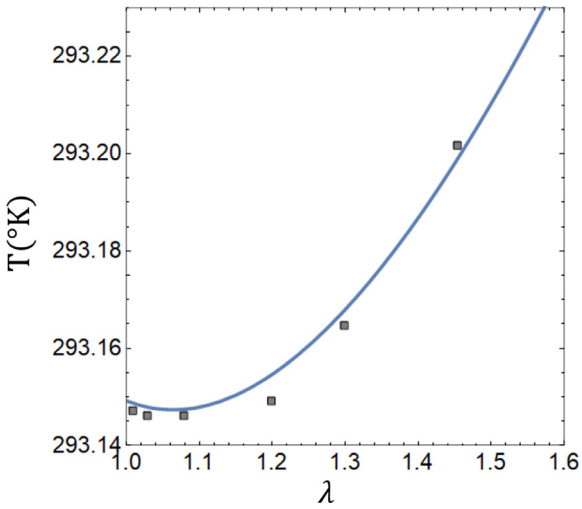

Fig. 5. Temperature versus stretch (for $\eta = -1.40042\,[\mathrm{MPa/K}]$); points designate Joule's experimental data (Joule et al., 1859).

Some authors (e.g. Holzapfel, 2000; Volokh, 2016) assume the constant heat capacity, $c = c_0$, corresponding to the following thermal energy: $Q(T) = c_0(T - T_0 - T\ln[T/T_0])$. This function is *concave yet negative*, which means the decrease of the thermal energy under the increase of the temperature. The latter property might be questionable.

In order to calibrate the initial heat capacity, c_0, we consider the problem of the inversion point, showing the dependence of temperature on uniaxial stretch for the fixed entropy. The entropy is calculated from the constitutive law with account of the thermoelastic incompressibility constraint (Volokh, 2016)

$$\eta = -\frac{\partial W}{\partial T} - \kappa\frac{\partial J}{\partial T}. \tag{26}$$

We choose the specific material data shown in Table 1 (Holzapfel, 2000) for the calibration of the initial heat capacity.

For an adiabatic stretching the entropy is constant and we assume a reference state for which $\lambda = 1$ at $T = 293.15$K. Substituting these values and the material constants from Table 1 in (26), we find a best fit curve to Joule's experimental data (Joule et al., 1859) for which: $c_0 = 1.4\,[\mathrm{MPa/K}]$ and $\eta = -1.40042\,[\mathrm{MPa/K}]$. The calibrated temperature-stretch diagram is shown in Fig. 5. The inversion point is reproduced by the theory in accordance with the experimental observations.

3.4. Calibration

The material parameters are found using a nonlinear least squares optimization method with the help of the *Lsqurvefit* tool in the Optimization Toolbox of MATLAB (MATLAB, 2017). The method minimizes the sum of the squared residuals. The residual, $res_i = \sigma_i^{\mathrm{test}} - \sigma_i^{\mathrm{fit}}$, is defined as the difference between the stresses of the test value, σ_i^{test}, and the fitted value, σ_i^{fit}, at a given stretch point λ_i. The error estimate is given by $S = \sum_{i=1}^{n} res_i^2$, where n is the number of stretch points included in the fit.

In the uniaxial case, the analytical stress-stretch relationships given in Section 3.2 represent the test directly and the experimental results can be straightforwardly compared to the analytical description for every stretch.

The case of biaxial tension is subtler. This test is routine when the intact behavior of material is examined. However, the biaxial tension test becomes very sensitive to imperfections when the specimen is stretched to failure and the homogeneous stress-stretch state turns to disadvantage rather than merit. In order to overcome the difficulties of the direct biaxial loading the bulge test is often used in the literature, e.g. Hamdi et al. (2006), Lev et al. (2018). In this test, material failure always starts on the top of the inflating membrane and it is not sensitive to boundary conditions. Unfortunately, there is a cost for such improvement of the experimental reliability - the stress-stretch state is not homogeneous and, consequently, the theoretical interpretation of the test results is not trivial.

Our idea is to find the equibiaxial stretches on the top of the inflating membrane. It cannot be done purely experimentally because any physical marks on the specimen would have finite length while the stretches of interest are pointwise. Instead, we choose a material model and its parameters and simulate the membrane inflation by using the finite element

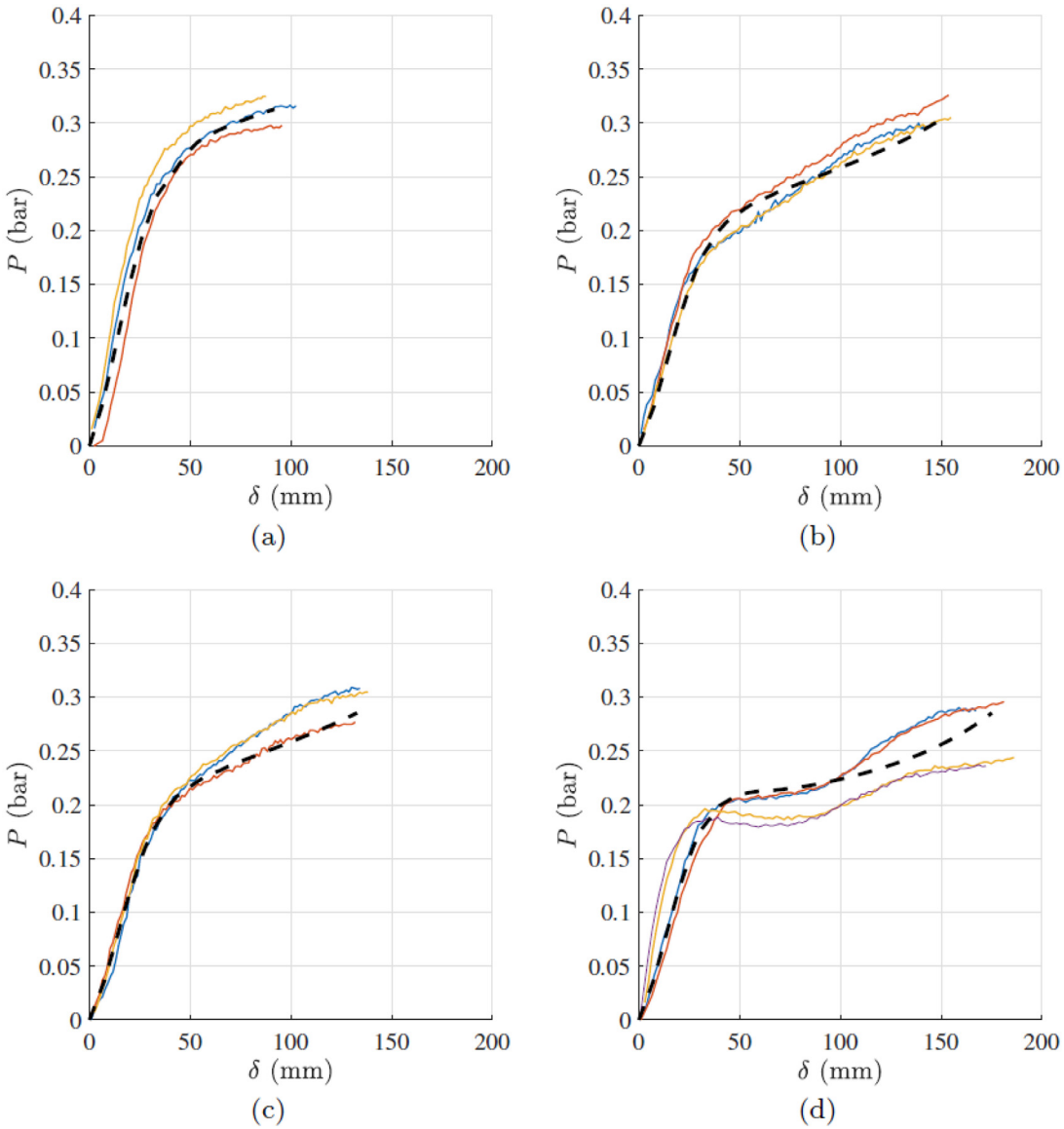

Fig. 6. Experimental $p-\delta$ curves for (a) Nitrile Butadiene Rubber at 70°C; (b) Neoprene at 50°C; (c) Neoprene at 90°C; and (d) Silicone at 25°C. Simulation results are shown in dashed lines.

method. In particular, we use quadrilateral three-node axisymmetric shell elements within ABAQUS (6.14) software. Material parameters are fitted by comparing simulations with experiments using the *Lsqurvefit* MATLAB tool. Examples of such fits up to the points of failure are shown in Fig. 6 where the internal balloon pressure, p, is tracked against the vertical displacement of the membrane pole, δ.

The material parameters are fitted for the intact three-term Ogden model. The stretches and stresses on the top of the membrane calculated for the experimentally fitted theoretical model are considered as the *experimental equibiaxial stretches*. In this, somewhat sophisticated, way we extract the purely equibiaxial data for the further fit of the theoretical models including failure.

Now, we can advance to a simultaneous uniaxial-equibiaxial fit of the material parameters. The the squared residuals are given by $S=\sum_{i=1}^{n}(res_u)_i^2+\sum_{i=1}^{n}(res_e)_i^2$, where residuals $res_u=\sigma_u^{\text{test}}-\sigma_u^{\text{fit}}$ and $res_e=\sigma_e^{\text{test}}-\sigma_e^{\text{fit}}$ are for the cases of uniaxial and equibiaxial tension accordingly. We emphasize again that σ_e^{test} is taken from the bulge test fit while σ_e^{fit} is calculated based on the formulas from Section 3.2.

Results of the simultaneous uniaxial and biaxial tension fit are presented in Table 2 and Figs. 7, 8 and 9 for Nitrile Butadiene Rubber, Neoprene, and Silicone accordingly.

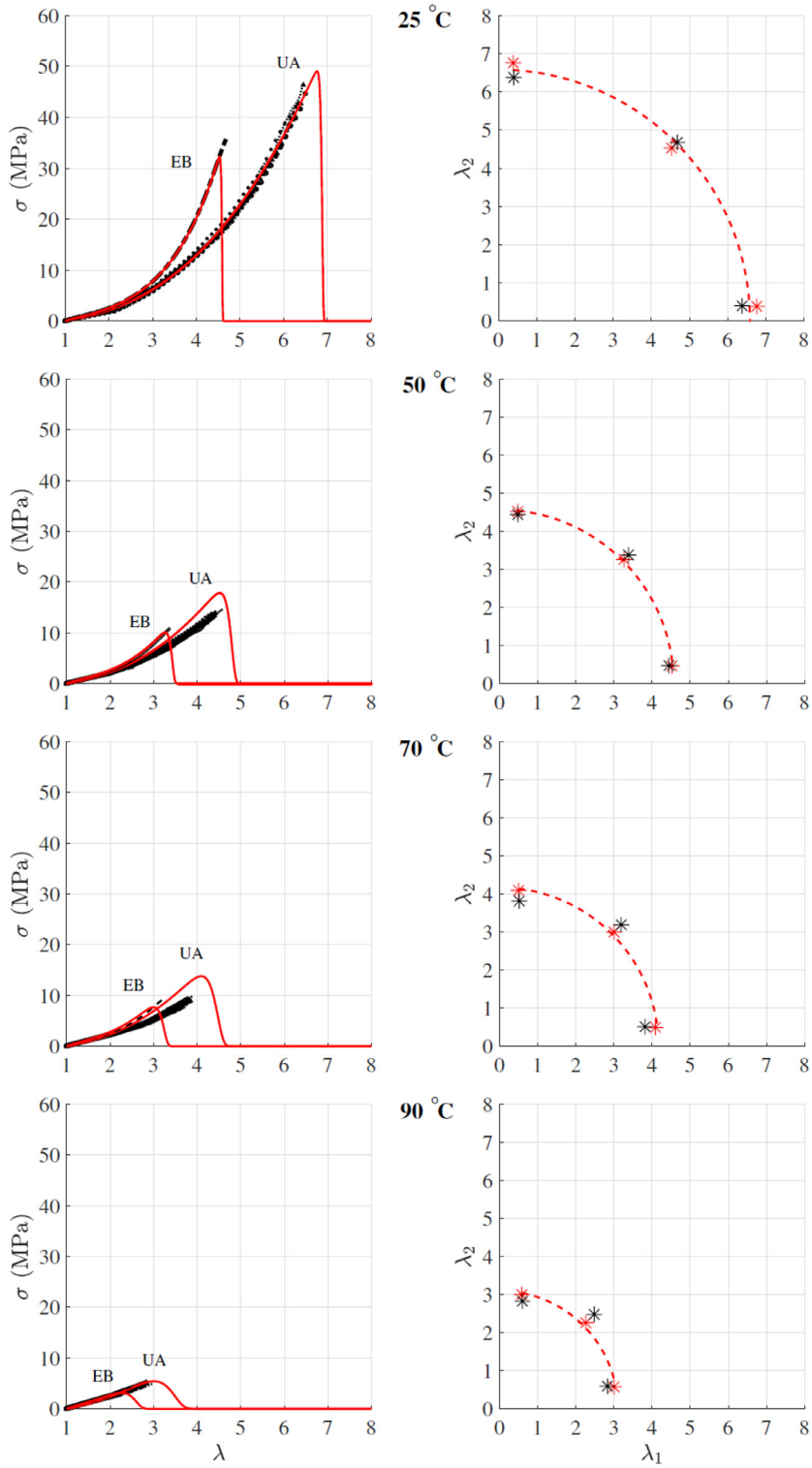

Fig. 7. On the left: Cauchy stress versus stretch for Nitrile Butadiene Rubber in uniaxial (UA) and equibiaxial (EB) tension at various temperatures; black points are for tests and solid red lines are for theory. On the right: Failure envelope; black for experiments and red for theory. (For interpretation of the references to color in this figure legend, the reader is referred to the web version of this article.)

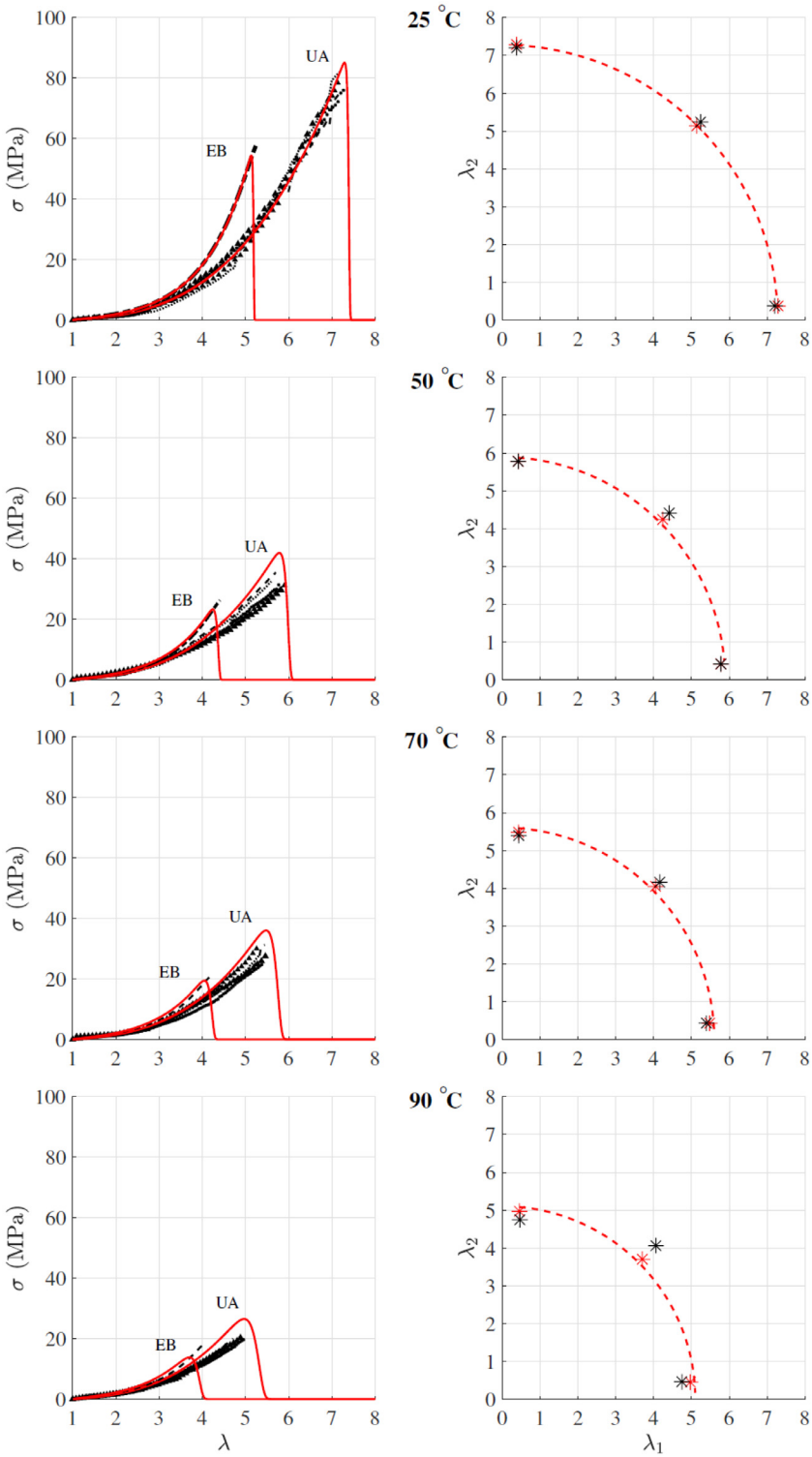

Fig. 8. On the left: Cauchy stress versus stretch for Neoprene in uniaxial (UA) and equibiaxial (EB) tension at various temperatures; black points are for tests and solid red lines are for theory. On the right: Failure envelope; black for experiments and red for theory. (For interpretation of the references to color in this figure legend, the reader is referred to the web version of this article.)

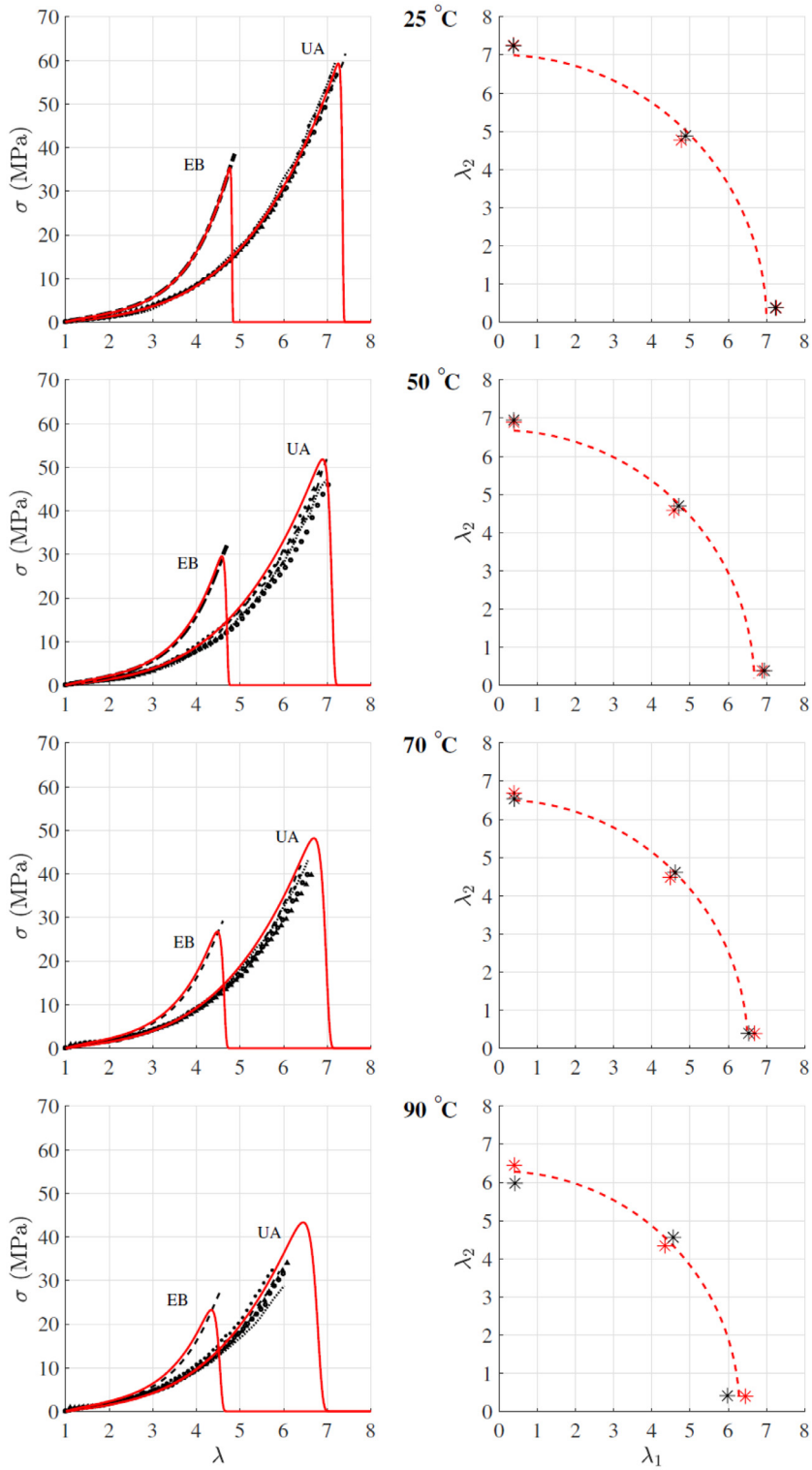

Fig. 9. On the left: Cauchy stress versus stretch for Silicone in uniaxial (UA) and equibiaxial (EB) tension at various temperatures; black points are for tests and solid red lines are for theory. On the right: Failure envelope; black for experiments and red for theory. (For interpretation of the references to color in this figure legend, the reader is referred to the web version of this article.)

Table 2
Material parameters for the three-term generalized thermoelastic Ogden model with energy limiters ($m = 100$).

	Nitrile Butadiene Rubber	Neoprene	Silicone
μ_1[MPa]	−3	$-1.674 \cdot 10^{-4}$	−0.0011
μ_2[MPa]	−0.002	−0.2729	5.0
μ_3[MPa]	0.3563	0.1356	0.046
α_1	−0.0498	−3.6384	−3.1414
α_2	−2.94	−0.7328	0.1387
α_3	2.5773	3.2445	3.6
ϕ[MPa] for 25°C	20	28	19
ϕ[MPa] for 50°C	42	49	52
ϕ[MPa] for 70°C	66	73	77
ϕ[MPa] for 90°C	86	94	100

Table 3
Material constants for the energy limiter function.

	Nitrile Butadiene Rubber	Neoprene	Silicone
ϕ_0[MPa]	20	28	19
β[MPa/K]	1.005	0.995	1.2655

The parameter m (see Eq. (2)), is a dimensionless parameter controlling the sharpness of transition to the material failure on the stress-strain curve (Volokh, 2007; 2010; 2013). Our tests show brittle failure behaviour for which we assume $m = 100$ for all calibrations. Further increase of this parameter does not affect results and the differences are negligible.

It is interesting to observe that the material stiffness is not very sensitive to the temperature alterations while the material strength can change significantly. The latter notion becomes very clear when the failure envelopes for various temperatures are placed on the same diagram - Fig. 10.

The strength of NBR is most affected by heat and the Silicone material is least affected. It can be observed that the most significant decrease in ultimate biaxial stretches occurs when temperature rises from 25°C to 50°C. For this case NBR and Neoprene ultimate stretches decrease by 30% and 19% respectively. Silicone shows a much better thermal resistance and its ultimate stretches decrease by 5% only.

We should also note that we considered the discrete values of the energy limiters at various temperatures. It can be readily observed - Fig. 11 - that these discrete values lie on the straight lines and, consequently, they can be described by a simple linear approximation

$$\phi(T) = \phi_0 + \beta(T - T_0), \tag{27}$$

where the energy limiter at the reference temperature ϕ_0 and material constant β are given in Table 3.

Fig. 11 presents a different behaviour compared to the energy limiter as function of temperature relation reported in Lev et al. (2018). This results from the different theory used for calibration. Here we use the new fully coupled thermoelastic theory developed.

4. Cavitation

In this section we apply the developed constitutive theory to the study of the cavitation problem. Unstable expansion of microscopic voids under remote hydrostatic tension is a typical failure scenario for many materials. There is a large body of the literature on this subject in general and for the hyperelastic materials (Ball, 1982; Cohen and Durban, 2010; Fond, 2001; Gent, 1990; Gent and Lindley, 1959; Henao, 2009; Horgan and Polignone, 1995; Lev and Volokh, 2016; Volokh, 2011; Williams and Schapery, 1965), in particular. Below, we generalize the cavitation analysis for the case of thermoelasticity, yet we restrict our considerations by the isothermal processes.

We use spherical coordinates r, φ, θ to describe the position of a generic material point in the current configuration, whose position in the initial configuration is described by coordinates R, Φ, Θ. We consider a very thick spherical shell with the initial internal and external radii A and B accordingly. The centrally-symmetric deformation has the form

$$r = r(R, T), \quad \varphi = \Phi, \quad \theta = \Theta. \tag{28}$$

In this case, the deformation gradient is diagonal and the principal stretches coincide with the stretches along the lines of the spherical coordinates. Thus, we have

$$\lambda_1 = \frac{\partial r}{\partial R}, \quad \lambda_2 = \lambda_3 = \frac{r}{R}, \tag{29}$$

where index 1 is for the radial direction and indices 2 and 3 are for the hoop directions.

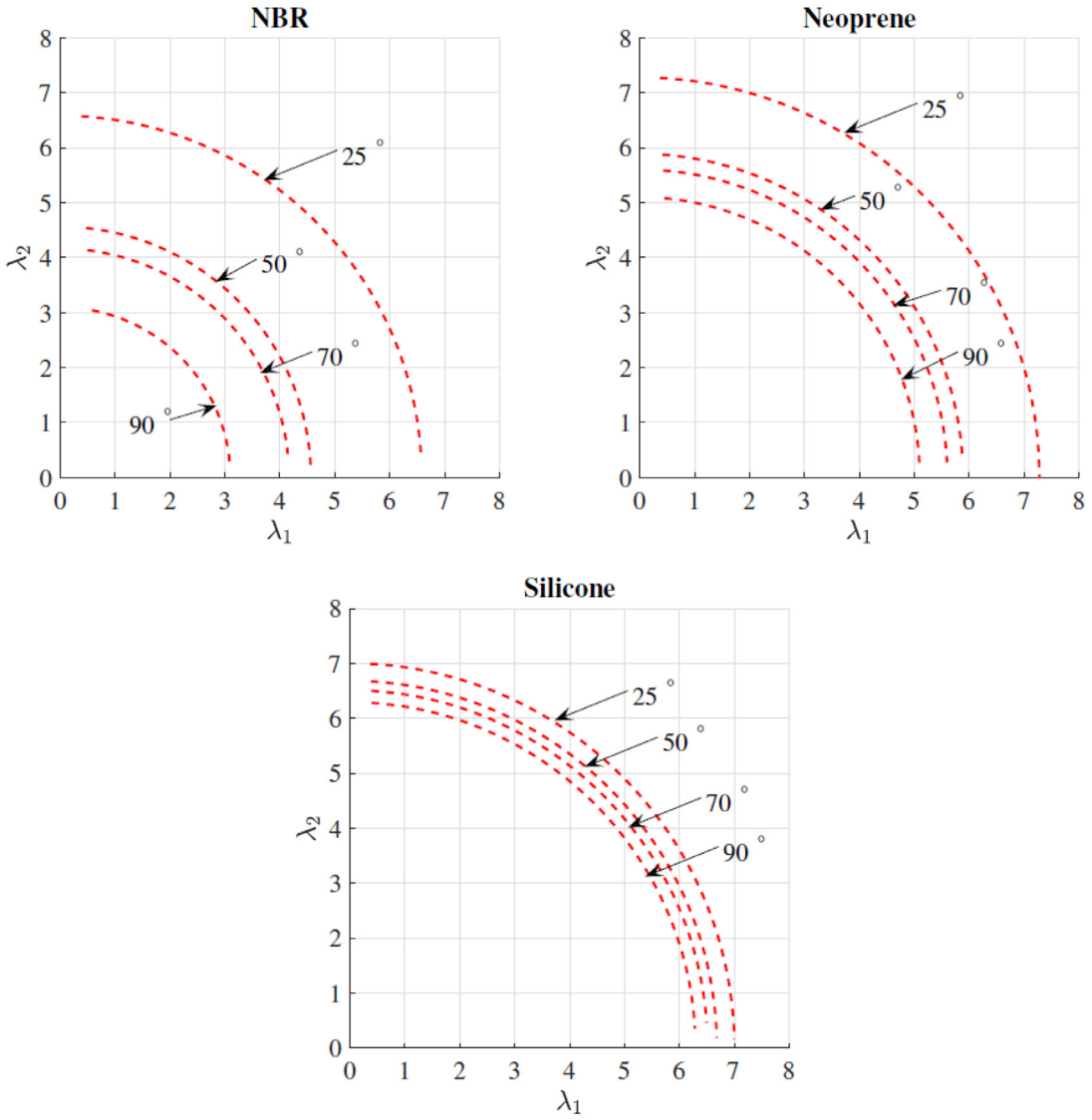

Fig. 10. Biaxial failure envelopes for considered materials.

Similarly, diagonal components of the Cauchy tensor are the principal stresses and the constitutive equations can be written in the following form

$$\sigma_1 = \sigma_{rr} = \lambda_1 \frac{\partial \psi}{\partial \lambda_1} - \kappa,$$
$$\sigma_2 = \sigma_{\varphi\varphi} = \lambda_2 \frac{\partial \psi}{\partial \lambda_2} - \kappa, \tag{30}$$
$$\sigma_3 = \sigma_{\theta\theta} = \lambda_3 \frac{\partial \psi}{\partial \lambda_3} - \kappa.$$

The stresses obey the equilibrium equation

$$\frac{\partial \sigma_1}{\partial r} + 2\frac{\sigma_1 - \sigma_2}{r} = 0, \tag{31}$$

and boundary conditions

$$\sigma_1(a) = 0, \quad \sigma_1(b) = g, \tag{32}$$

where g is the hydrostatic tension and $a = r(A)$ and $b = r(B)$ are the internal and the external radii of the sphere after the deformation.

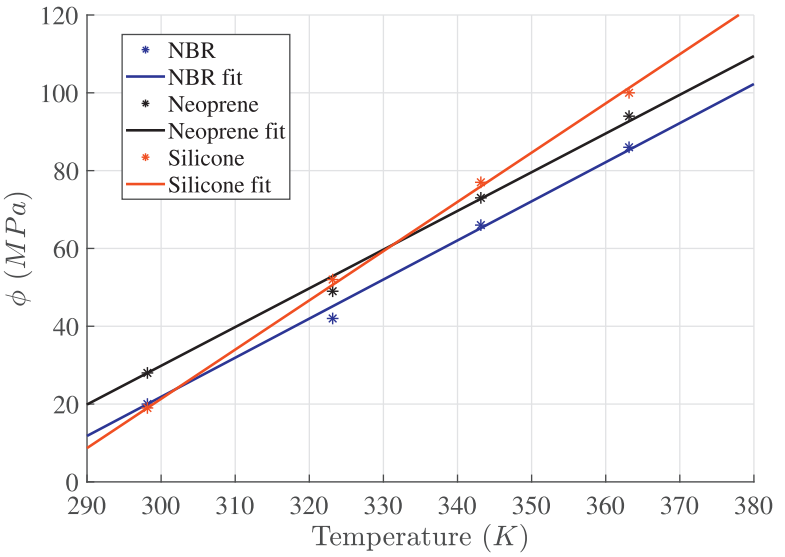

Fig. 11. Energy limiter as a function of the temperature.

We note that the thermoelastic incompressibility condition

$$\lambda_1\lambda_2\lambda_3 = \frac{\partial r}{\partial R}\frac{r^2}{R^2} = J(T) \tag{33}$$

can be integrated and we can get the deformation law in the form

$$r^3 - a^3 = J(R^3 - A^3). \tag{34}$$

Then, we have

$$\lambda \equiv r/R = (J^{-1} - J^{-1}a^3r^{-3} + A^3r^{-3})^{-1/3}, \tag{35}$$

and

$$\lambda_1 = J\lambda^{-2}, \quad \lambda_2 = \lambda_3 = \lambda. \tag{36}$$

By using the chain rule for differentiation, we can rewrite the equilibrium equation in the form

$$r\frac{\partial\lambda}{\partial r}\frac{\partial\sigma_1}{\partial\lambda} = 2(\sigma_2 - \sigma_1), \tag{37}$$

and calculate the factor on the left hand side of this equation as follows

$$\begin{aligned} r\partial\lambda/\partial r &= -r(J^{-1} - J^{-1}a^3r^{-3} + A^3r^{-3})^{-4/3}(J^{-1}3a^3r^{-4} - 3A^3r^{-4})/3 \\ &= (J^{-1} - J^{-1}a^3r^{-3} + A^3r^{-3})^{-4/3}(J^{-1} - J^{-1}a^3r^{-3} + A^3r^{-3} - J^{-1}) \\ &= \lambda^4(\lambda^{-3} - J^{-1}). \end{aligned} \tag{38}$$

We also introduce the reduced Helmholtz free energy function

$$\bar{\psi}(\lambda, T) = \psi(J\lambda^{-2}, \lambda, \lambda, T) \tag{39}$$

and calculate

$$\begin{aligned} \partial\bar{\psi}/\partial\lambda &= (\partial\psi/\partial\lambda_i)(\partial\lambda_i/\partial\lambda) \\ &= -2J\lambda^{-3}\partial\psi/\partial\lambda_1 + \partial\psi/\partial\lambda_2 + \partial\psi/\partial\lambda_3 \\ &= -2\lambda^{-1}(\sigma_1 + \kappa) + 2\lambda^{-1}(\sigma_2 + \kappa) \\ &= 2\lambda^{-1}(\sigma_2 - \sigma_1), \end{aligned} \tag{40}$$

or

$$2(\sigma_2 - \sigma_1) = \lambda\partial\bar{\psi}/\partial\lambda. \tag{41}$$

Back substitution of (38) and (41) in (37) yields

$$\frac{\partial\sigma_1}{\partial\lambda} = \frac{1}{1 - \lambda^3J^{-1}}\frac{\partial\bar{\psi}}{\partial\lambda}. \tag{42}$$

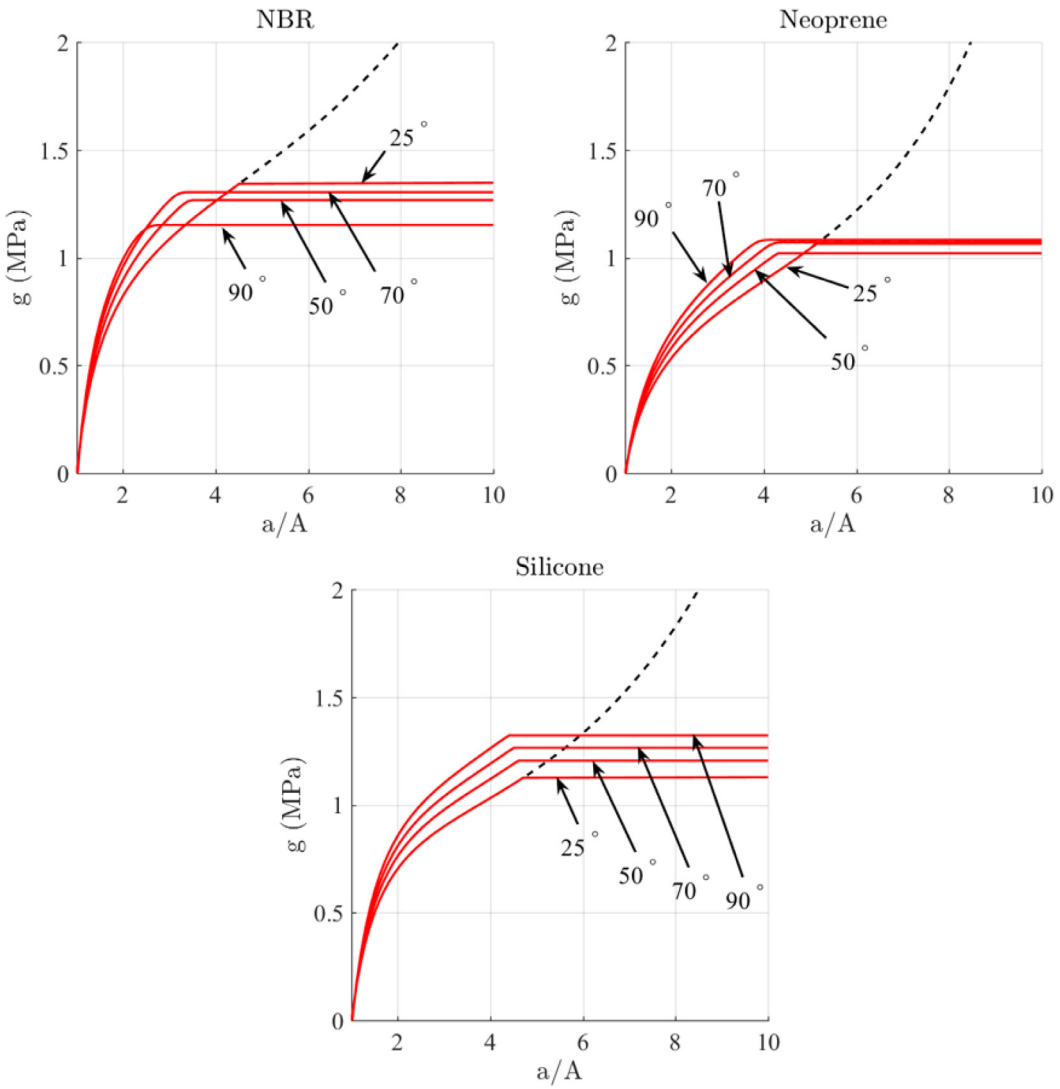

Fig. 12. Hydrostatic tension versus normalized void radius for three materials. Dashed lines show the intact material behavior without the energy limiter.

Integrating this equation from $\lambda_a = a/A$ to $\lambda_b = b/B$ and accounting for the boundary conditions (32) we get

$$g = \int_{\lambda_b}^{\lambda_a} \frac{\partial \bar{\psi}/\partial \lambda}{\lambda^3 J^{-1} - 1} d\lambda. \tag{43}$$

Finally, we assume that there is no stretching far from the cavity $\lambda_b = 1$ while the cavity boundary can expand and we get

$$g(\lambda_a, T) = \int_{1}^{\lambda_a} \frac{\partial \bar{\psi}/\partial \lambda}{\lambda^3 J^{-1} - 1} d\lambda. \tag{44}$$

Calculations based on the developed formula are presented graphically in Fig. 12.

Horizontal lines in Fig. 12 represent the unstable expansion of voids - cavitation. This instability is a material failure phenomenon and it would not appear in the absence of the failure description within the constitutive model (energy limiter). It is interesting that the critical stretch (horizontal axis) of the onset of cavitation always decreases with the increasing temperature while the critical hydrostatic tension (vertical axis) might increase as in the case of Silicone. Such slight increase in the critical tension can be explained by the increase of the material stiffness with heating. In the case of NBR, the drop of the critical stretch is so pronounced (Fig. 10) that the temperature-dependent material stiffening cannot elevate the critical cavitation tension.

5. Conclusions

Experiments, theory, and application concerning the coupled thermo-mechanical behavior of rubberlike materials have been considered in the present study.

Experiments have been done on Nitrile Butadiene Rubber, Neoprene, and Silicone for various temperatures in the range from 20°C to 90°C. The experiments included the tracking of deformation and failure of the rubberlike materials in uniaxial and equibiaxial tension. The latter was done indirectly by using the bulge test in which a thin specimen membrane was inflated up to rupture. A methodology was developed for the interpretation of the experimental results based on the finite element simulations with the iterative fit of material constants. The equibiaxial stress-stretch state at the pole of the inflated membrane was used for further calibration of the material model. The latter calibration was based on the simultaneous fit of uniaxial and equibiaxial data.

Constitutive theories have been developed to describe the thermoelastic behavior of rubberlike materials. Energy limiters, depending on the temperature were introduced in the Helmholtz free energy in order to describe material failure. The Ogden three-term hyperelastic model was generalized to include the thermal energy. A new form of the thermal energy was proposed in $(24)_3$, which was concave yet positive. The theoretical model was calibrated for Nitrile Butadiene Rubber, Neoprene, and Silicone.

As opposed to our previous work (Lev et al., 2018) that includes only bulge tests, here we add uniaxial tests that serve as a validation of the results. Biaxial failure envelopes are build from the ultimate stretches obtained from our two independent test configurations (Hamdi et al., 2006). The calibration is done simultaneously to fit both data sets. Only few papers present simultaneous calibration using multiple test data (Ogden et al., 2004). The calibration is done using a new coupled thermo-elastic theory, which leads to a new energy limiter as function of temperature relation (Eq. (27) and Fig. 11). The circular biaxial failure envelopes can be found in the literature only for room temperature (Hamdi et al., 2006). The circular envelopes for different temperatures (Fig. 10) are novel and offers an immediate view of material thermal resistance. Envelopes that are close together are thermally resistant while envelopes that are apart are less resistant.

Application of the constitutive theories to analysis of cavitation problem has been considered. A new simple formula for thermoelastic cavitation (44) was developed and applied to Nitrile Butadiene Rubber, Neoprene, and Silicone. It was found that the onset of cavitation was affected by the interplay between the reduced material strength and the increased material stiffness as a result of heating.

Summarizing the most interesting results in one sentence we would conclude that the stiffness of rubberlike materials only slightly depends on the temperature alterations while the strength might be significantly decreased by heating, depending on the specific material.

Acknowledgment

The support from the Israel Science Foundation (ISF-198/15) and the Israel Ministry of Construction are gratefully acknowledged. The authors are also grateful to Ofir Barak for the help in preparation of the LabVIEW interface for the experimental setup.

References

Aboudi, J., 2002. Micromechanical analysis of the fully coupled finite thermoelastic response of rubber-like matrix composites. Int. J. Solids Struct. 39 (9), 2587–2612.
Gent, A., 2001. Engineering with Rubber: How to Design Rubber Components.
ASTM, 2007. Standard Test Methods for Vulcanized Rubber and Thermoplastic Elastomers-Tension, d 412-06a. New York: American National Standards Institute.
Balakhovsky, K., Volokh, K.Y., 2012. Inflation and rupture of rubber membrane. Int. J. Fract. 177 (2), 179–190.
Ball, J.M., 1982. Discontinuous equilibrium solutions and cavitation in nonlinear elasticity. Philos. Trans. R. Soc. Lond. A 306 (1496), 557–611.
Chadwick, P., 1974. Thermo-mechanics of rubberlike materials. Philos. Trans. R. Soc. Lond. A 276 (1260), 371–403.
Chadwick, P., Creasy, C., 1984. Modified entropic elasticity of rubberlike materials. J. Mech. Phys. Solids 32 (5), 337–357.
Charalambides, M.N., Wanigasooriya, L., Williams, G.J., Chakrabarti, S., 2002. Biaxial deformation of dough using the bubble inflation technique. i. experimental. Rheol. Acta 41 (6), 532–540.
Cohen, T., Durban, D., 2010. Cavitation in elastic and hyperelastic sheets. Int. J. Eng. Sci. 48 (1), 52–66.
Dickie, R.A., Smith, T.L., 1969. Ultimate tensile properties of elastomers. VI. strength and extensibility of a styrene–butadiene rubber vulcanizate in equal biaxial tension. J. Polym. Sci. Part B: Polym. Phys. 7 (4), 687–707.
Fond, C., 2001. Cavitation criterion for rubber materials: a review of void-growth models. J. Polym. Sci. Part B: Polym. Phys. 39 (17), 2081–2096.
Fried, I., 1982. Finite element computation of large rubber membrane deformations. Int. J. Numer. Methods Eng. 18 (5), 653–660.
Gent, A., 1990. Cavitation in rubber: a cautionary tale. Rubber Chem. Technol. 63 (3), 49–53.
Gent, A., Lindley, P., 1959. Internal rupture of bonded rubber cylinders in tension. Proc. R. Soc. Lond. A 249, 195–205.
Hamdi, A., Abdelaziz, M.N., Hocine, N.A., Heuillet, P., Benseddiq, N., 2006. A fracture criterion of rubber-like materials under plane stress conditions. Polym. Test. 25 (8), 994–1005.
Henao, D., 2009. Cavitation, invertibility, and convergence of regularized minimizers in nonlinear elasticity. J. Elast. 94 (1), 55.
Holzapfel, A.G., 2000. Nonlinear Solid Mechanics. John Wiley & Sons, Inc..
Horgan, C., Polignone, D., 1995. Cavitation in nonlinearly elastic solids: a review. Appl. Mech. Rev. 48 (8), 471–485.
Joule, J.P., et al., 1859. V. on some thermo-dynamic properties of solids. Philos. Trans. R. Soc.Lond. 149, 91–131.
Lev, Y., Faye, A., Volokh, K.Y., 2018. Experimental study of the effect of temperature on strength and extensibility of rubberlike materials. Exp. Mech. 58 (5), 847–858.
Lev, Y., Volokh, K.Y., 2016. On cavitation in rubberlike materials. J. Appl. Mech. 83 (4), 044501.
Marckmann, G., Verron, E., 2006. Comparison of hyperelastic models for rubber-like materials. Rubber Chem. Technol. 79 (5), 835–858.

MATLAB, 2017. Optimization Toolbox: User's Guide, Version R2017b. MathWorks.
Morman Jr, K.N., 1995. A Thermomechanical Model for Amorphous Polymers in the Glassy Transition and Rubber Regions. Technical Report. University of California, Los Angeles, CA, United States.
Ogden, R., 1992. On the thermoelastic modeling of rubberlike solids. J. Therm. Stresses 15 (4), 533–557.
Ogden, R., Saccomandi, G., Sgura, I., 2004. Fitting hyperelastic models to experimental data. Comput. Mech. 34 (6), 484–502.
Ogden, R.W., 1972. Large deformation isotropic elasticity–on the correlation of theory and experiment for incompressible rubberlike solids. Proc. R. Soc. Lond. A 326, 565–584.
Ogden, R.W., 1997. Non-linear Elastic Deformations. Dover.
Rodgers, B., 2015. Rubber Compounding: Chemistry and Applications, Second Edition CRC Press.
Saccomandi, G., Ogden, R.W., 2004. Mechanics and Thermomechanics of Rubberlike Solids, 452. Springer.
Sasso, M., Palmieri, G., Chiappini, G., Amodio, D., 2008. Characterization of hyperelastic rubber-like materials by biaxial and uniaxial stretching tests based on optical methods. Polym. Test. 27 (8), 995–1004.
Vahapoglu, V., Karadeniz, S., Yazici, I., 2011. Uniaxial tensile testing of rubber-like materials. Exp. Tech. 35 (1), 17–23.
Volokh, K.Y., 2007. Hyperelasticity with softening for modeling materials failure. J. Mech. Phys. Solids 55 (10), 2237–2264.
Volokh, K.Y., 2010. On modeling failure of rubber-like materials. Mech. Res. Commun. 37 (8), 684–689.
Volokh, K.Y., 2011. Cavitation instability in rubber. Int. J. Appl. Mech. 3 (02), 299–311.
Volokh, K.Y., 2013. Review of the energy limiters approach to modeling failure of rubber. Rubber Chem. Technol. 86 (3), 470–487.
Volokh, K.Y., 2014. On irreversibility and dissipation in hyperelasticity with softening. J. Appl. Mech. 81 (7), 074501.
Volokh, K.Y., 2015. Non-linear thermoelasticity with energy limiters. Int. J. Non Linear Mech. 76, 169–175.
Volokh, K.Y., 2016. Mechanics of Soft Materials. Springer.
Williams, M., Schapery, R., 1965. Spherical flaw instability in hydrostatic tension. Int. J. Fract.Mech. 1 (1), 64–72.